Available online at www.sciencedirect.com
SCIENCE DIRECT®
Physics of the Earth and Planetary Interiors 139 (2003) 113–127
PHYSICS OF THE EARTH AND PLANETARY INTERIORS
www.elsevier.com/locate/pepi

Atomistic simulations of trace element incorporation into the large site of $MgSiO_3$ and $CaSiO_3$ perovskites

Alexandre Corgne [a,*], Neil L. Allan [b], Bernard J. Wood [a]

[a] *CETSEI, Department of Earth Sciences, University of Bristol, Wills Memorial Building, Bristol BS8 1RJ, UK*
[b] *School of Chemistry, University of Bristol, Cantock's Close, Bristol BS8 1TS, UK*

Received 18 October 2002; received in revised form 13 March 2003; accepted 14 March 2003

Abstract

We have used computer simulation techniques to study the mechanisms of trace element incorporation into the large sites of $MgSiO_3$ and $CaSiO_3$ perovskites on the atomistic level. Both relaxation and solution energies corresponding to the incorporation of isovalent and heterovalent defects can be fitted using the 'lattice strain' model. This underlines the importance of crystal chemistry in the partitioning of trace elements between perovskite and melt. As expected, solution energies, which take some account of possible melt components, approximate more closely experimental perovskite–melt partitioning observations than do relaxation energies. With calculated solution energies we find that the optimum site radius r_0 decreases with increasing defect charge while the apparent Young's modulus E_α of the large site increases with charge in both perovskites, consistent with experimental perovskite–melt partitioning data. For a given trace element charge r_0 is smaller for $MgSiO_3$ than for $CaSiO_3$, as observed experimentally. For a given trace element the difference in calculated solution energy between the two perovskites is reflected in the difference in experimental partition coefficients. For all the charge balancing mechanisms we have considered the solution energies for REE^{3+}, and 4+ cations (including U^{4+} and Th^{4+}) are much lower in $CaSiO_3$ perovskite than in $MgSiO_3$ perovskite, which provides an explanation for the observed ease with which $CaSiO_3$ perovskite accommodates 3+ and 4+ cations.

Keywords: Perovskite; Lower mantle; Trace element partitioning; Substitution mechanisms; Atomistic simulation

1. Introduction

The earth is generally considered to have accreted from planetesimal-sized bodies whose impact energies increased as the earth grew, culminating with the giant impact which led to the moon formation (e.g., Hartmann and Davis, 1975). Under most scenarios the energy of accretion and differentiation was sufficient to generate a deep magma ocean (e.g., Herzberg and O'Hara, 1985; Ohtani, 1985), and perhaps to melt the entire silicate earth. Crystallisation of such a deep magma ocean has been suggested as a mechanism for enriching the lower mantle in Si by the gravitational settling of perovskite (Ringwood, 1979). But the difficulty with this hypothesis is that it is required to take place without significantly changing the ratios of relative abundance of refractory lithophile elements in the primitive upper mantle. Recent partitioning experiments (Corgne and Wood, 2002; Hirose et al., in press) have shown that a mixture of $CaSiO_3$ and $MgSiO_3$ perovskites fractionated during early earth history must represent only a few percent of the mantle

* Corresponding author. Tel.: +44-117-954-5245; fax: +44-117-925-3385.
E-mail address: alexandre.corgne@bris.ac.uk (A. Corgne).

0031-9201/$ – see front matter © 2003 Elsevier B.V. All rights reserved.
doi:10.1016/S0031-9201(03)00148-1

volume to maintain chondritic ratios of refractory lithophile elements in the primitive upper mantle. Depending on the proportion of $CaSiO_3$ perovskite, the corresponding perovskitic reservoir could be enriched in U and Th and thus contribute to the earth's heat budget, but in any case it would not be large enough to explain the observed Si depletion of the primitive upper mantle. Although these estimates do not account for the fractionation of magnesiowüstite, which is the liquidus phase in the upper part of the lower mantle, it seems highly improbable that there is a large perovskitic layer hidden in the deep lower mantle.

As underlined by these conclusions, the partitioning of trace elements between perovskite and melt are of considerable importance to the understanding of the geochemical differentiation of the earth. A proper evaluation of the role of perovskite in the distribution of trace elements in the deep mantle requires detailed knowledge of the physico-chemical factors controlling perovskite–melt partitioning. In this paper, we report atomistic computer simulations of trace element incorporation in $MgSiO_3$ and $CaSiO_3$ perovskites. As undertaken for other silicates in previous studies (e.g., Purton et al., 1996, 1997; Van Westrenen et al., 2000), such simulations provide insight into the energetics of substitution into perovskites on an atomic scale. We compare results from our simulations with recent experimental observations in order to obtain a detailed understanding at the atomistic level of the controlling factors in perovskite–melt partitioning.

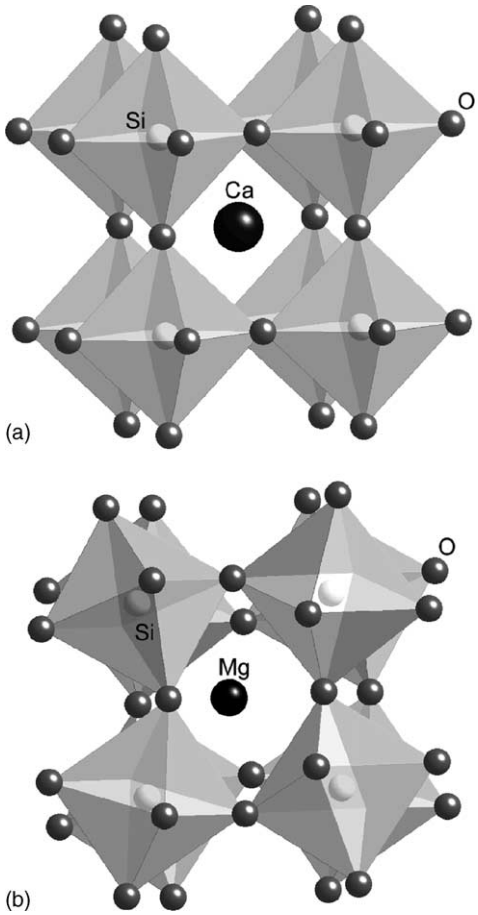

Fig. 1. Crystal structure of (a) $CaSiO_3$ perovskite and (b) $MgSiO_3$ perovskite. Note the distortion from a cubic ($Pm\bar{3}m$) to an orthorhombic (*Pbnm*) structure.

2. Theoretical and experimental background

As shown in Fig. 1, $CaSiO_3$ and $MgSiO_3$ perovskites have different structures. $CaSiO_3$ perovskite adopts the cubic $Pm\bar{3}m$ structure at least up to depths of 2300 km (Shim et al., 2000). This high-symmetry structure contains two cation sites, an octahedral B-site occupied by Si (6-fold coordinated) and a regular dodecahedral A-site occupied by Ca (12-fold coordinated). X-ray diffraction patterns of temperature-quenched samples confirm $MgSiO_3$ perovskite has a distorted orthorhombic *Pbnm* structure at pressures up to 127 GPa (Knittle and Jeanloz, 1987). This orthorhombic structure is associated with tilting of the BO_6 octahedra in the cubic structure, such that 8 of the 12 A-site nearest-neighbours in the cubic structure are closer to the Mg ion than the remaining four.

The 'lattice strain' model of Brice (1975) (see also Blundy and Wood, 1994) relates the lattice strain energy U_{strain} associated with the insertion of an isovalent misfit cation of radius r_i into a spherical site with radius r_0, to the elasticity of the site (apparent Young's modulus, E_α) and the size misfit ($r_i - r_0$) between defect and host cations:

$$U_{strain} = 4\pi E_\alpha N_A[\tfrac{1}{2} r_0 (r_i - r_0)^2 + \tfrac{1}{3}(r_i - r_0)^3] \quad (1)$$

where N_A is the Avogadro's number. The larger the size misfit, or the lower the site elasticity (the higher E_α), the higher the strain energy associated with a

substitution, and the lower the affinity of the host structure for a particular trace element. Because crystals are far more rigid than melts, the energy involved in the melt–crystal exchange reaction is dominated by the strain energy in the crystal. Thus the substituting trace element which produces the highest strain energy is the most incompatible. For heterovalent substitution, expressions of the form of Eq. (1) also fit experimental trace element partitioning data, the fitted values of E_α and r_0 being generally different from those derived from isovalent substitution.

Following previous work on a range of silicates (e.g., Blundy and Wood, 1994; Van Westrenen et al., 1999; Hill et al., 2000), Corgne and Wood (2002) successfully applied the 'lattice strain' model to $CaSiO_3$ perovskite–melt partitioning of a wide range of trace elements and we present here similar preliminary results for $MgSiO_3$ perovskite–melt partitioning (Fig. 2, Table 1). For the large site (A-site: Ca- or Mg-site) of both perovskites, the optimum radius r_0 decreases as the charge of the incorporated cation increases. Such a variation had already been observed for garnets and wollastonite (Van Westrenen et al., 1999; Law et al., 2000). While for the large site of $MgSiO_3$

Table 1
$MgSiO_3$ perovskite–melt partition coefficients[a]

Mg	1.19 (4)
Ca	0.27 (3)
Sr	0.0091 (69)
Ga	0.55 (9)
Sc	2.14 (48)
Lu	0.98 (8)
Yb	0.93 (7)
Er	0.50 (5)
Y	0.42 (5)
Ho	0.37 (5)
Gd	0.18 (5)
Eu	0.10 (2)
Sm	0.062 (26)
Nd	0.038 (18)
Pr	0.031 (7)
Ce	0.015 (7)
La	0.0086 (64)
Hf	0.94 (14)
Zr	1.19 (19)
U	0.027 (7)
Th	0.021 (8)

[a] The preliminary data are from a melting experiment on a peridotite composition at 25 GPa and 2300 °C. Values in parentheses are two standard errors in terms of least units cited.

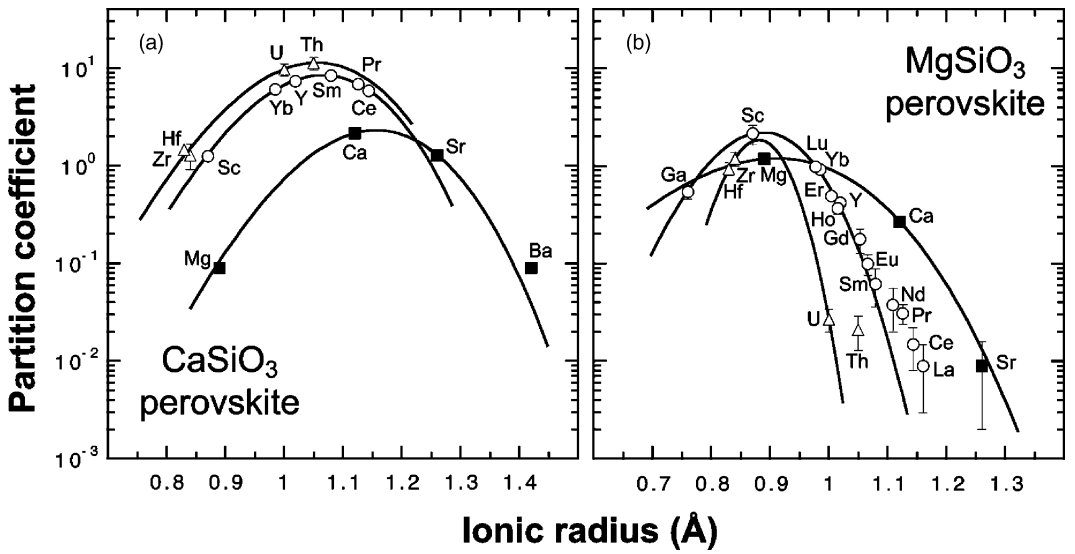

Fig. 2. 'Lattice strain' model fits to experimental data (25 GPa and 2300 °C) of (a) $CaSiO_3$ perovskite–melt partitioning (data from Corgne and Wood, 2002) and (b) $MgSiO_3$ perovskite–melt partitioning (preliminary data, see Table 1). Ionic radii used in this study are taken from Shannon (1976). Since ionic radii are not available for the whole set of elements in 12-fold coordination, we have taken values corresponding to a 8-fold coordinated site for $CaSiO_3$ perovskite. The radius of Al in 8-fold coordination (0.67 Å) was estimated by extrapolation of values available for lower coordination.

perovskite E_α increases as the charge on the defect cation increases, for $CaSiO_3$ perovskite E_α shows no significant variation with trace element charge. Another interesting observation is that the optimum partition coefficients ${D_0}^{3+}$ and ${D_0}^{4+}$ for the large site differ substantially between $MgSiO_3$ and $CaSiO_3$ perovskites. The main goal of this study is therefore to explain the differences between the experimental results in terms of the energetics involved in trace element partitioning.

3. Simulation methodology

The details of atomistic simulation techniques, which are based on energy minimisation procedures, have been described elsewhere (e.g., Catlow and Mackrodt, 1982; Allan et al., 2001, 2003) and we only present a short summary. All atomistic simulations were performed in a static system (zero pressure, zero temperature) using the general utility lattice program (GULP, Gale, 1997). Calculations used a Born ionic model, in which formal charges are assigned to spherical ions based on accepted chemical valence and electron counting (e.g., 2+ for Ca and Mg, 4+ for Si, 2− for O). The lattice energy U_{lat} is partitioned into a Coulombic term, corresponding to long-range electrostatic interactions between atoms, and a non-Coulombic term, corresponding to short-range repulsions produced by the overlap of nearest-neighbour electron clouds. To describe non-Coulombic interactions between adjacent ions we used the set of potentials given in Table 2. Cation–oxygen interactions are described by 2-body Buckingham potentials. The shell model of Dick and Overhauser (1958) was used to take account of the oxide ion polarisation and a 3-body O–Si–O bond bending term was incorporated. Previous studies have shown the applicability of these potentials for simulation of oxides and silicates (e.g., Wright and Price, 1993; Purton et al., 1996, 1997; Van Westrenen et al., 2000; Watson et al., 2000). Simulated structures for $MgSiO_3$ and $CaSiO_3$ perovskites, the calculated lattice parameters of which were reproduced to within 1% of the experimental values (Table 3), were used as a basis for defect energy calculations. In every computational run, one or more defects were introduced into the $ASiO_3$ crystal lattice. Initial, unrelaxed defect energies $U_{\text{def,i}}$ were calculated without allowing any atoms to move. The total energy of the defective system was then minimised by allowing the surrounding ions to relax to accommodate the misfit cation(s). Positions of cores and shells of atoms around the defect(s) were optimised using the customary two-region approach (Catlow and Mackrodt, 1982). In the inner region (9 Å radius), the lattice relaxation is largest and the elastic force equations are solved requiring that the force on all ions in this region must be zero. In the outer region (16 Å radius), the lattice relaxation was assumed to be smaller and was estimated using the Mott–Littleton approximation (Mott and Littleton, 1938). The number of ions used for each structure is sufficient to ensure convergence of defect energies with region size. At convergence, final, relaxed defect energies $U_{\text{def,f}}$ were obtained. The energy released as the surrounding ions move to accommodate the substituting cation, the relaxation energy U_{rel}, is defined as $U_{\text{def,i}} - U_{\text{def,f}}$. U_{rel}, which is always positive, is equivalent to U_{strain} in Eq. (1). Although our simulations are in the static limit, defect energies in this limit have been shown to be a good approximation to defect enthalpies at elevated temperatures (Taylor et al., 1997).

Relaxation energies are a function of the crystal properties only. In a crystal–melt system, however, partitioning of a particular trace element schematically involves: (1) the removal of the element from the melt; (2) its incorporation into the crystal structure by a substitution mechanism; (3) the insertion of the host cation into the melt. The calculation of solution energies, in which some attempt is made to assess the influence of the melt, should therefore provide a better representation of the energetics involved in mineral–melt trace element partitioning than the relaxation energies alone. For isovalent substitutions into $ASiO_3$ perovskite, stages (1)–(3) can be described by the following reaction, using the conventional Kröger–Vink notation (Kröger and Vink, 1956; see also Allan et al., 2003):

$$\mathrm{MO} + \mathrm{A_A} \Leftrightarrow \mathrm{M_A} + \mathrm{AO} \tag{2a}$$

$$U_{\text{sol}} = U_{\text{def,f}}(\mathrm{M_A}) + U_{\text{lat}}(\mathrm{MO}) - U_{\text{lat}}(\mathrm{AO}) \tag{2b}$$

Solution energies have been approximated by assuming that, in the melt, the host and defect cations have environments similar to those in the corresponding solid simple oxides (Purton et al., 1996). Explicit

Table 2
Interatomic potentials parameters and calculated lattice energies[a]

Interactions	Ref.	A (kJ mol^{-1})	ρ (Å)	C (kJ mol^{-1})	U_{lat}[b] (kJ mol^{-1})
Li^{+}–O_{shell}	Purton et al. (1997)	25331	0.3476		−2868
Na^{+}–O_{shell}	Purton et al. (1997)	122231	0.3065		−2533
K^{+}–O_{shell}	Purton et al. (1997)	65652	0.3798		−2171
Rb^{+}–O_{shell}	Purton et al. (1997)	88706	0.3772		−2090
Ni^{2+}–O_{shell}	Lewis and Catlow (1985)	152688	0.2882		−4022
Mg^{2+}–O_{shell}	Lewis and Catlow (1985)	137829	0.2945		−3986
Co^{2+}–O_{shell}	Lewis and Catlow (1985)	143927	0.2951		−3948
Fe^{2+}–O_{shell}	Lewis and Catlow (1985)	116515	0.3084		−3880
Mn^{2+}–O_{shell}	Lewis and Catlow (1985)	97199	0.3262		−3743
Ca^{2+}–O_{shell}	Lewis and Catlow (1985)	105207	0.3437		−3469
Eu^{2+}–O_{shell}	Purton et al. (1996)	120462	0.3556		−3258
Sr^{2+}–O_{shell}	Purton et al. (1996)	132667	0.3500		−3269
Ba^{2+}–O_{shell}	Lewis and Catlow (1985)	89895	0.3949		−3023
Al^{3+}–O_{shell}	Lewis and Catlow (1985)	107572	0.3118		−15534
Cr^{3+}–O_{shell}	Lewis and Catlow (1985)	167315	0.3010		−14886
Fe^{3+}–O_{shell}	Lewis and Catlow (1985)	106365	0.3299		−14509
Sc^{3+}–O_{shell}	Lewis and Catlow (1985)	125373	0.3312		−14017
Lu^{3+}–O_{shell}	Lewis and Catlow (1985)	129975	0.3430		−13341
Yb^{3+}–O_{shell}	Lewis and Catlow (1985)	126357	0.3462		−13262
Ho^{3+}–O_{shell}	Lewis and Catlow (1985)	130274	0.3487		−13073
Gd^{3+}–O_{shell}	Lewis and Catlow (1985)	128981	0.3551		−12813
Eu^{3+}–O_{shell}	Lewis and Catlow (1985)	131027	0.3556		−12754
Nd^{3+}–O_{shell}	Lewis and Catlow (1985)	133140	0.3601		−12527
Pr^{3+}–O_{shell}	Buscaglia et al. (2001)	139440	0.3608		−12382
La^{3+}–O_{shell}	Lewis and Catlow (1985)	138910	0.3651		−12228
Si^{4+}–O_{shell}	Sanders et al. (1984)	123878	0.3205	1028	−12419
Ge^{4+}–O_{shell}	Lewis and Catlow (1985)	99910	0.3464		−11640
Ti^{4+}–O_{shell}	Lewis and Catlow (1985)	72769	0.3879		−10856
Sn^{4+}–O_{shell}	Lewis and Catlow (1985)	90570	0.3813		−10542
Tb^{4+}–O_{shell}	Lewis and Catlow (1985)	87348	0.3949		−10143
Ce^{4+}–O_{shell}	Lewis and Catlow (1985)	97797	0.3949		−9908
U^{4+}–O_{shell}	Lewis and Catlow (1985)	101840	0.3949		−9827
Th^{4+}–O_{shell}	Lewis and Catlow (1985)	110736	0.3949		−9665
O_{shell}–O_{shell}	Sanders et al. (1984)	2196384	0.1490	2690	
O_{core}–O_{shell}	Purton et al. (1996)	Spring constant $k = 7229$ kJ mol^{-1} Å^{-2}			
O_{shell}–Si–O_{shell}	Sanders et al. (1984)	Spring constant $K_B = 202$ kJ mol^{-1} rad^{-2}			

[a] Interatomic potentials are of the form $V(r) = A\exp(-r/\rho) - C/r^6$, where r is the interionic distance (2-body) and $V(\theta) = [K_B(\theta - \pi/2)^2]/2$, where θ is the O–Si–O bond angle (3-body). Oxygen core–shell interactions are given by $kx^2/2$, where x is the core–shell separation. Core charge and shell charge for O are +0.86902 and −2.86902, respectively. A short-range cutoff of 12 Å was used throughout.
[b] Calculated lattice energies are for corresponding binary oxides.

inclusion of the heats of fusion of these oxides (Aylward and Findlay, 1994) makes little difference. Clearly, the calculation of solution energy (Eq. (2b)) involves the final defect energy ($U_{def,f}$) and the difference in lattice energy (U_{lat}) of the trace and host element oxides. Lattice energies of oxides calculated using GULP are listed in Table 2. For heterovalent substitutions, reactions corresponding to (2a) and (2b) are made more complex by the presence of charge balancing substitutions, which are required to maintain electroneutrality. In this case, one or more defects were introduced simultaneously into the crystal, as near as possible to the first defect. Purton et al. (1997) have demonstrated the importance of defect association in forsterite and diopside, and have shown that defect energies are not additive and cannot be predicted simply from the separate defect energies for the isolated defects. Therefore, we present results here only for

Table 3
Comparison between calculated and experimental lattice parameters

Perovskite	Structure	Source	a (Å)	b (Å)	c (Å)	α (°)	β (°)	γ (°)
$MgSiO_3$	*Pbnm*	Simulation	4.8244	4.8454	6.8416	90.0	89.9	90.5
		Experiment[a]	4.7787	4.9313	6.9083	90	90	90
$CaSiO_3$	$Pm\bar{3}m$	Simulation	3.599			90.0		
		Experiment[b]	3.572			90		

[a] Horiuchi et al. (1987).
[b] Wang et al. (1996).

associated defects. The exact position in the crystal lattice of the surrounding charge balancing defect(s) was varied in order to find the lowest final defect energy.

For monovalent cations substituting at the large A-site, the envisaged compensation mechanisms are formation of oxygen vacancies (Eq. (3)) and associated substitution into the A-site involving a trivalent defect (Eq. (4)):

$$\tfrac{1}{2}M_2O + A_A + \tfrac{1}{2}O_O \Leftrightarrow M'_A + \tfrac{1}{2}V^{\bullet\bullet}_O + AO \quad (3a)$$

$$U_{sol} = \tfrac{1}{2}U_{def,f}(2M'_A + V^{\bullet\bullet}_O) + U_{lat}(AO) - \tfrac{1}{2}U_{lat}(M_2O) \quad (3b)$$

$$\tfrac{1}{2}M_2O + \tfrac{1}{2}J_2O_3 + 2A_A \Leftrightarrow M'_A + J^{\bullet}_A + 2AO \quad (4a)$$

$$U_{sol} = U_{def,f}(M'_A + J^{\bullet}_A) + 2U_{lat}(AO) - \tfrac{1}{2}U_{lat}(M_2O) - \tfrac{1}{2}U_{lat}(J_2O_3) \quad (4b)$$

For trivalent substitutions at the large site, four different incorporation mechanisms have been investigated. In the first type, the trivalent defect is compensated by a monovalent defect (Eq. (4)). In the second and third types (Eqs. (5) and (6)), charge compensation occurs by formation of A- and Si-vacancies, respectively. In the fourth type (Eq. (7)), the trivalent defect at the A-site is associated with Al-substitution at the Si-site:

$$\tfrac{1}{2}M_2O_3 + \tfrac{3}{2}A_A \Leftrightarrow M^{\bullet}_A + \tfrac{1}{2}V''_A + \tfrac{3}{2}AO \quad (5a)$$

$$U_{sol} = \tfrac{1}{2}U_{def,f}(2M^{\bullet}_A + V''_A) + \tfrac{3}{2}U_{lat}(AO) - \tfrac{1}{2}U_{lat}(M_2O_3) \quad (5b)$$

$$\tfrac{1}{2}M_2O_3 + A_A + \tfrac{1}{4}Si_{Si} \Leftrightarrow M^{\bullet}_A + \tfrac{1}{4}V''''_{Si} + AO + \tfrac{1}{4}SiO_2 \quad (6a)$$

$$U_{sol} = \tfrac{1}{4}U_{def,f}(4M^{\bullet}_A + V''''_{Si}) + U_{lat}(AO) + \tfrac{1}{4}U_{lat}(SiO_2) - \tfrac{1}{2}U_{lat}(M_2O_3) \quad (6b)$$

$$\tfrac{1}{2}M_2O_3 + \tfrac{1}{2}Al_2O_3 + A_A + Si_{Si} \Leftrightarrow M^{\bullet}_A + Al'_{Si} + AO + SiO_2 \quad (7a)$$

$$U_{sol} = U_{def,f}(M^{\bullet}_A + Al'_{Si}) + U_{lat}(AO) + U_{lat}(SiO_2) - \tfrac{1}{2}U_{lat}(M_2O_3) - \tfrac{1}{2}U_{lat}(Al_2O_3) \quad (7b)$$

In the case of tetravalent substitutions, we envisaged four mechanisms of charge compensation. The first two mechanisms involve the formation of A- and Si-vacancies, respectively (Eqs. (8) and (9)), whereas the third and fourth mechanisms involve the substitution of Si by a divalent cation (Ca for $CaSiO_3$ and Mg for $MgSiO_3$) and Al, respectively (Eqs. (10) and (11)):

$$MO_2 + 2A_A \Leftrightarrow M^{\bullet\bullet}_A + V''_A + 2AO \quad (8a)$$

$$U_{sol} = U_{def,f}(M^{\bullet\bullet}_A + V''_A) + 2U_{lat}(AO) - U_{lat}(MO_2) \quad (8b)$$

$$MO_2 + A_A + \tfrac{1}{2}Si_{Si} \Leftrightarrow M^{\bullet\bullet}_A + \tfrac{1}{2}V''''_{Si} + AO + \tfrac{1}{2}SiO_2 \quad (9a)$$

$$U_{sol} = \tfrac{1}{2}U_{def,f}(2M^{\bullet\bullet}_A + V''''_{Si}) + U_{lat}(AO) + \tfrac{1}{2}U_{lat}(SiO_2) - U_{lat}(MO_2) \quad (9b)$$

$$MO_2 + A_A + Si_{Si} \Leftrightarrow M^{\bullet\bullet}_A + A''_{Si} + SiO_2 \quad (10a)$$

$$U_{sol} = U_{def,f}(M^{\bullet\bullet}_A + A''_{Si}) + U_{lat}(SiO_2) - U_{lat}(MO_2) \quad (10b)$$

$$MO_2 + Al_2O_3 + A_A + 2Si_{Si} \Leftrightarrow M_A^{\bullet\bullet} + 2Al'_{Si} + AO + 2SiO_2 \quad (11a)$$

$$U_{sol} = U_{def,f}(M_A^{\bullet\bullet} + 2Al'_{Si}) + U_{lat}(AO) + 2U_{lat}(SiO_2) - U_{lat}(MO_2) - U_{lat}(Al_2O_3) \quad (11b)$$

4. Relaxation energies

Initial and final defect energies ($U_{def,i}$ and $U_{def,f}$) and relaxation energies (U_{rel}) for all the envisaged substitutions are listed in Table 4. As noted by Purton et al. (1996, 1997) and Van Westrenen et al. (2000), there is an approximately linear increase in $U_{def,f}$ for a given valence with increasing trace element radius. The lowest relaxation energies are plotted against trace element radius in Fig. 3. We caution that the lowest relaxation energies are not necessarily those associated with the lowest energy substitutions. For each isovalent series of trace elements, U_{rel} exhibits a near-parabolic dependence on the ionic radius. Since GULP simulations do not involve the use of any concept of ionic radius, such an observation provides evidence for the general applicability of the 'lattice strain' model equation (Eq. (1)) to relaxation energies in defective perovskite lattices. Thus each series was fitted using this equation. Regression parameters E_α and r_0 are presented in Table 4. As expected from crystal chemistry considerations, $r_0(CaSiO_3) > r_0(MgSiO_3)$, with $r_0{}^{2+}$ being almost equal to the radius of the host cation, i.e., r_{Ca} for $CaSiO_3$ perovskite and r_{Mg} for $MgSiO_3$ perovskite. As found for other minerals and oxides (Purton et al., 1996, 1997; Van Westrenen et al., 2000), r_0 increases with defect charge. This trend is opposite to that observed in mineral–melt partitioning experiments. The variation of relaxation energy with charge has been discussed by Van Westrenen et al. (2000).

From the viewpoint of site elasticity, the fits to the lattice strain model suggest $E_\alpha(MgSiO_3) > E_\alpha(CaSiO_3)$ for a given valence, which is expected because the Ca–O bond is more compressible than the Mg–O bond. Like r_0, E_α increases with defect charge in both perovskites. The trend in E_α is consistent with the experimental work on $MgSiO_3$ perovskite. However, given our findings regarding the incorrect variation of r_0 with defect charge, we now turn to consider calculated solution energies which, unlike relaxation energies, do take some account of the melt environment.

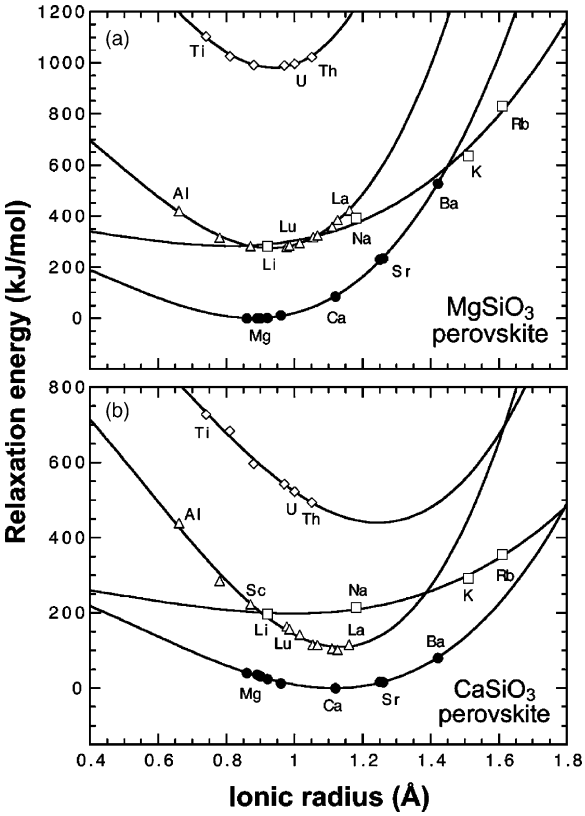

Fig. 3. Calculated relaxation energies for trace element incorporation in (a) $MgSiO_3$ and (b) $CaSiO_3$ perovskite. Curves are least-squares fits to data of the 'lattice strain' model (Eq. (1)). Data and regression parameters E_α and r_0 are listed in Table 4.

5. Solution energies

5.1. Favoured substitution mechanisms

Solution energies (U_{sol}) for all the envisaged substitutions are listed in Table 4. The preferred substitution mechanism (i.e., the one leading to the lowest U_{sol} values) for monovalent incorporation at the large A-site is coupled trivalent substitution at the A-site for both perovskites, except for K and Rb which have lowest solution energy associated with oxygen vacancy in $MgSiO_3$. For trivalent incorporation into

Table 4
Defect, relaxation and solution energies in $MgSiO_3$ and $CaSiO_3$ perovskites[a]

Substitution at the A-site	$MgSiO_3$ perovskite				$CaSiO_3$ perovskite			
	$U_{def,i}$	$U_{def,f}$	U_{rel}	U_{sol}	$U_{def,i}$	$U_{def,f}$	U_{rel}	U_{sol}
	1 + defects							
$Li_A^+ + \frac{1}{2}V_O$	3094	2706	388	154	2578	2182	396	147
$Na_A^+ + \frac{1}{2}V_O$	3384	2920	464	201	2726	2333	393	131
$K_A^+ + \frac{1}{2}V_O$	4179	3491	688	**591**	3295	2847	448	464
$Rb_A^+ + \frac{1}{2}V_O$	4587	3753	834	**812**	3556	3052	504	628
r_0 (Å)			0.84 (15)	**0.99 (1)**			1.11 (6)	1.06 (4)
E_α (GPa)			145 (46)	**321 (7)**			83 (24)	317 (45)
	$M^{3+} = Sc$				$M^{3+} = Lu$			
$Li_A^+ + M_A^{3+}$	−54	−337	282	**134**	−956	−1154	198	**12**
$Na_A^+ + M_A^{3+}$	275	−116	391	**187**	−794	−1008	214	**−9**
$K_A^+ + M_{3A}^+$	1164	527	637	649	−175	−469	293	**349**
$Rb_A^+ + M_{3A}^+$	1623	791	831	873	110	−246	356	**531**
r_0 (Å)			0.81 (30)	**0.97 (3)**			1.00 (10)	**1.07 (3)**
E_α (GPa)			163 (98)	**345 (34)**			76 (24)	**351 (44)**
	2 + defects							
Ni_A^{2+}	−37	−37	0	**−1**	−506	−546	40	**7**
Mg_A^{2+}	0	0	0	**0**	−482	−518	36	**−1**
Co_A^{2+}	34	33	0	**−5**	−464	−496	32	**−17**
Fe_A^{2+}	113	111	2	**5**	−409	−434	25	**−23**
Mn_A^{2+}	284	272	12	**29**	−295	−308	13	**−34**
Ca_A^{2+}	751	666	85	**149**	0	0	0	**0**
Eu_A^{2+}	1322	1092	229	**364**	364	347	17	**136**
Sr_A^{2+}	1306	1071	235	**354**	343	326	16	**126**
Ba_A^{2+}	2294	1766	527	**803**	971	890	81	**444**
r_0 (Å)			0.88 (1)	**0.86 (2)**			1.12(−)	**1.00 (1)**
E_α (GPa)			385 (8)	**543 (30)**			176 (7)	**557 (24)**
	3 + defects							
	$M^+ = Li^+$				$M^+ = Na^+$			
$Al_A^{3+} + M_A^+$	−590	−1011	421	**218**	−1367	−1828	461	268
$Fe_A^{3+} + M_A^+$	−265	−580	315	**136**	−1163	−1479	316	104
$Sc_A^{3+} + M_A^+$	−54	−337	283	**133**	−1040	−1312	272	25
$Lu_A^{3+} + M_A^+$	332	50	281	**183**	−794	−1008	214	−9
$Yb_A^{3+} + M_A^+$	388	104	284	**197**	−755	−962	208	−3
$Ho_A^{3+} + M_A^+$	523	228	295	**226**	−669	−862	193	3
$Gd_A^{3+} + M_A^+$	731	414	317	283	−530	−706	176	29
$Eu_A^{3+} + M_A^+$	782	457	325	296	−498	−670	172	35
$Nd_A^{3+} + M_A^+$	993	635	358	360	−359	−520	161	72
$Pr_A^{3+} + M_A^+$	1129	743	386	396	−274	−430	156	90
$La_A^{3+} + M_A^+$	1309	888	421	464	−152	−304	152	139
r_0 (Å)			0.93 (1)	**0.84 (1)**			1.16 (3)	0.97 (1)
E_α (GPa)			688 (18)	**837 (28)**			366 (45)	977 (17)

Table 4 (*Continued*)

Substitution at the A-site	$MgSiO_3$ perovskite				$CaSiO_3$ perovskite			
	$U_{def,i}$	$U_{def,f}$	U_{rel}	U_{sol}	$U_{def,i}$	$U_{def,f}$	U_{rel}	U_{sol}
$Al_A^{3+} + \frac{1}{2}V_A$	−938	−1512	574	276	−1763	−2202	439	362
$Fe_A^{3+} + \frac{1}{2}V_A$	−612	−1068	456	208	−1559	−1844	285	207
$Sc_A^{3+} + \frac{1}{2}V_A$	−401	−821	420	208	−1436	−1659	223	146
$Lu_A^{3+} + \frac{1}{2}V_A$	−16	−432	416	260	−1190	−1353	164	114
$Yb_A^{3+} + \frac{1}{2}V_A$	40	−378	418	274	−1150	−1308	158	120
$Ho_A^{3+} + \frac{1}{2}V_A$	176	−254	430	303	−1065	−1208	143	125
$Gd_A^{3+} + \frac{1}{2}V_A$	384	−68	452	360	−925	−1043	117	160
$Eu_A^{3+} + \frac{1}{2}V_A$	435	−25	460	373	−894	−1008	115	165
$Nd_A^{3+} + \frac{1}{2}V_A$	645	152	493	436	−755	−861	106	199
$Pr_A^{3+} + \frac{1}{2}V_A$	782	259	523	471	−670	−772	103	215
$La_A^{3+} + \frac{1}{2}V_A$	962	403	559	538	−548	−663	116	247
r_0 (Å)			0.94 (1)	0.83 (1)			1.13 (2)	0.96 (1)
E_α (GPa)			737 (21)	786 (24)			460 (43)	881 (36)
$Al_A^{3+} + \frac{1}{4}V_{Si}$	585	−428	1014	248	393	−915	1308	278
$Fe_A^{3+} + \frac{1}{4}V_{Si}$	911	12	899	176	597	−557	1154	124
$Sc_A^{3+} + \frac{1}{4}V_{Si}$	1121	250	871	168	721	−377	1098	58
$Lu_A^{3+} + \frac{1}{4}V_{Si}$	1507	616	891	196	966	−96	1063	0
$Yb_A^{3+} + \frac{1}{4}V_{Si}$	1563	666	897	206	1006	−56	1061	2
$Ho_A^{3+} + \frac{1}{4}V_{Si}$	1698	780	918	**226**	1091	34	1057	−3
$Gd_A^{3+} + \frac{1}{4}V_{Si}$	1907	953	954	**268**	1231	174	1057	7
$Eu_A^{3+} + \frac{1}{4}V_{Si}$	1957	992	966	**278**	1262	204	1059	7
$Nd_A^{3+} + \frac{1}{4}V_{Si}$	2168	1155	1013	**327**	1401	337	1064	27
$Pr_A^{3+} + \frac{1}{4}V_{Si}$	2305	1253	1052	**353**	1486	414	1073	31
$La_A^{3+} + \frac{1}{4}V_{Si}$	2485	1385	1099	**409**	1608	518	1090	58
r_0 (Å)			0.90 (1)	**0.86** (**1**)			1.03 (1)	1.02 (1)
E_α (GPa)			843 (27)	**683** (**17**)			606 (40)	731 (19)
$Al_A^{3+} + Al_{Si}^{3+}$	1634	1119	515	248	1199	585	614	**231**
$Fe_A^{3+} + Al_{Si}^{3+}$	1959	1552	407	168	1403	933	470	**67**
$Sc_A^{3+} + Al_{Si}^{3+}$	2170	1796	374	167	1527	1096	431	**−17**
$Lu_A^{3+} + Al_{Si}^{3+}$	2582	2186	395	219	1772	1392	380	**−58**
$Yb_A^{3+} + Al_{Si}^{3+}$	2612	2236	375	229	1812	1437	375	**−53**
$Ho_A^{3+} + Al_{Si}^{3+}$	2747	2360	387	258	1897	1534	363	**−50**
$Gd_A^{3+} + Al_{Si}^{3+}$	2981	2547	434	316	2037	1686	350	**−28**
$Eu_A^{3+} + Al_{Si}^{3+}$	3032	2590	442	329	2068	1721	348	**−23**
$Nd_A^{3+} + Al_{Si}^{3+}$	3243	2766	477	391	2207	1866	341	**9**
$Pr_A^{3+} + Al_{Si}^{3+}$	3353	2871	482	424	2293	1954	339	**24**
$La_A^{3+} + Al_{Si}^{3+}$	3533	3015	518	491	2414	2075	339	**68**
r_0 (Å)			0.92 (1)	0.84 (1)			1.12 (2)	**0.98** (**1**)
E_α (GPa)			671 (52)	809 (29)			396 (47)	**942** (**16**)
	4 + defects							
$Ti_A^{4+} + V_A$	−967	−2339	1372	545	−2645	−3372	727	546
$Sn_A^{4+} + V_A$	−731	−2023	1292	547	−2508	−3191	684	413
$Tb_A^{4+} + V_A$	−305	−1558	1253	613	−2205	−2802	597	403
$Ce_A^{4+} + V_A$	9	−1237	1246	699	−2002	−2545	543	425

Table 4 (*Continued*)

Substitution at the A-site	$MgSiO_3$ perovskite				$CaSiO_3$ perovskite			
	$U_{def,i}$	$U_{def,f}$	U_{rel}	U_{sol}	$U_{def,i}$	$U_{def,f}$	U_{rel}	U_{sol}
$U_A^{4+} + V_A$	131	−1119	1250	736	−1923	−2447	523	442
$Th_A^{4+} + V_A$	398	−873	1271	820	−1751	−2244	494	483
r_0 (Å)			0.95 (1)	0.69 (5)			1.25 (16)	0.91 (1)
E_α (GPa)			952 (90)	637 (137)			333 (158)	1468 (329)
$Ti_A^{4+} + \frac{1}{2}V_{Si}$	1916	−212	2128	**448**	1577	−944	2522	233
$Sn_A^{4+} + \frac{1}{2}V_{Si}$	2103	97	2006	**443**	1715	−687	2402	177
$Tb_A^{4+} + \frac{1}{2}V_{Si}$	2529	533	1996	**481**	2018	−330	2348	134
$Ce_A^{4+} + \frac{1}{2}V_{Si}$	2843	832	2011	**545**	2221	−100	2320	130
$U_A^{4+} + \frac{1}{2}V_{Si}$	2965	940	2025	**571**	2299	−21	2320	128
$Th_A^{4+} + \frac{1}{2}V_{Si}$	3232	1163	2069	**632**	2472	157	2314	144
r_0 (Å)			0.92 (1)	**0.74** (**2**)			0.99 (2)	0.96 (1)
E_α (GPa)			1378 (278)	**558** (**84**)			1093 (223)	692 (64)
$Ti_A^{4+} + A_{Si}$	3817	2022	1795	459	4438	1855	2584	292
$Sn_A^{4+} + A_{Si}$	4053	2339	1715	462	4576	2039	2537	162
$Tb_A^{4+} + A_{Si}$	4479	2793	1687	517	4879	2398	2481	122
$Ce_A^{4+} + A_{Si}$	4794	3103	1690	592	5082	2630	2451	119
$U_A^{4+} + A_{Si}$	4915	3216	1699	624	5160	2716	2445	124
$Th_A^{4+} + A_{Si}$	5183	3452	1731	698	5333	2900	2433	146
r_0 (Å)			0.93 (1)	0.70 (4)			1.06 (3)	0.95 (1)
E_α (GPa)			1024 (105)	563 (107)			455 (76)	1344 (250)
$Ti_A^{4+} + 2Al_{Si}^{3+}$	3997	2892	1105	458	3072	2147	925	**230**
$Sn_A^{4+} + 2Al_{Si}^{3+}$	4233	3207	1026	459	3209	2349	860	**118**
$Tb_A^{4+} + 2Al_{Si}^{3+}$	4659	3667	992	520	3512	2719	793	**89**
$Ce_A^{4+} + 2Al_{Si}^{3+}$	4974	3983	991	601	3715	2962	753	**97**
$U_A^{4+} + 2Al_{Si}^{3+}$	5095	4098	997	635	3794	3053	741	**107**
$Th_A^{4+} + 2Al_{Si}^{3+}$	5363	4339	1023	714	3967	3243	723	**135**
r_0 (Å)			0.94 (1)	0.70 (4)			1.08 (3)	**0.93** (**1**)
E_α (GPa)			978 (97)	607 (128)			545 (81)	**1249** (**224**)

[a] Values in parentheses are one standard deviation. Energies are given in kJ/mol. Favoured mechanisms are in bold.

the A-site, in $MgSiO_3$ perovskite, coupled monovalent substitution at the A-site is lowest in energy for heavy REE^{3+}, Al^{3+}, Fe^{3+}, and Sc^{3+}, whereas for light REE^{3+}, Si-vacancy formation is favoured. For $CaSiO_3$ perovskite, trivalent cation incorporation coupled to Al-substitution at the Si-site is preferred. For tetravalent incorporation, the lowest energy mechanism is Si-vacancy formation in $MgSiO_3$ perovskite, and, as for trivalent cations, coupled Al-substitution at the Si-site for $CaSiO_3$ perovskite. Nevertheless the difference in solution energy between the envisaged substitution mechanisms is often small (Table 4), which suggests that in both perovskites a range of different charge balancing mechanisms for 1+, 3+ and 4+ cations are possible. It is therefore difficult to conclude in favour of only one mechanism. Compensation via Ca-vacancy formation seems unlikely for incorporation of 3+ and 4+ cations into $CaSiO_3$ perovskite.

An important observation is that, whatever the substitution mechanism we consider, rare earth elements (REE^{3+}), U^{4+} and Th^{4+} have solution energies which are much lower for $CaSiO_3$ perovskite than for $MgSiO_3$ perovskite. This is a consequence both of $U_{def,f}$ ($CaSiO_3$) being more negative than

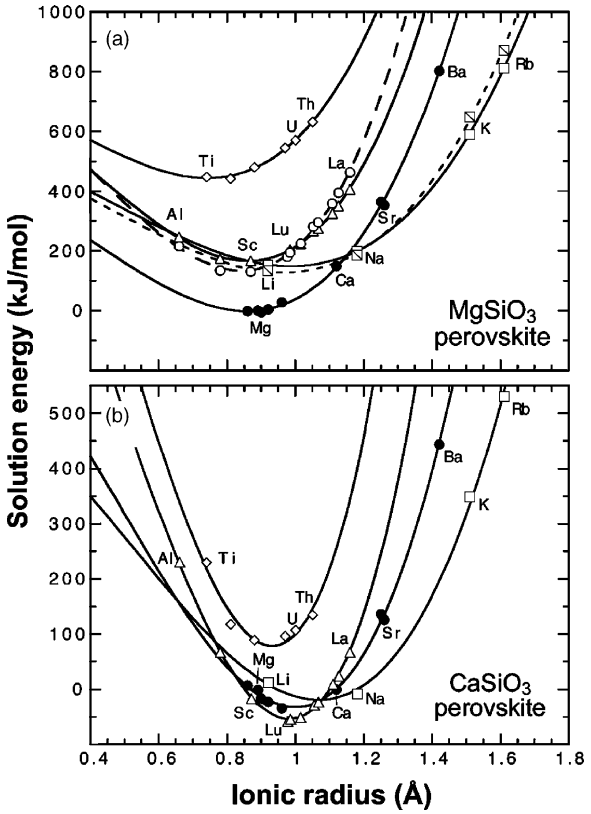

Fig. 4. Calculated solution energies for trace element incorporation in (a) $MgSiO_3$ and (b) $CaSiO_3$ perovskite. Curves are least-squares fits to data of the 'lattice strain' model (Eq. (1)). Data and regression parameters E_α and r_0 are listed in Table 4. Two substitution mechanisms have been considered for monovalent incorporation in $MgSiO_3$ perovskite. Depending on ionic radius, coupled trivalent substitution at the Mg-site (crossed square) or O-vacancy formation (open square) is preferred. Similarly, two substitution mechanisms have been considered for trivalent incorporation in $MgSiO_3$ perovskite. Depending on ionic radius, coupled monovalent substitution at the Mg-site (open circle) or Si-vacancy formation (open triangle) is preferred.

$U_{def,f}$ ($MgSiO_3$) and the difference in lattice energies between $CaSiO_3$ and $MgSiO_3$. Interestingly, this result is consistent with experimental observations, which show that REE^{3+}, U^{4+} and Th^{4+} are preferentially incorporated into $CaSiO_3$ perovskite relative to $MgSiO_3$ perovskite (Fig. 2). Such a conclusion, which could not be drawn from the consideration of relaxation energies alone, underlines the general agreement between simulated solution energies and experimental partitioning data.

5.2. Crystal chemistry considerations

Solution energies associated with the lowest energy substitutions are plotted against trace element radius in Fig. 4. As for relaxation energies, solution energies show clearly a near-parabolic dependence on ionic radius, stressing the control of local crystal environment on trace element partitioning. Regression parameters for fitted U_{sol} data to the 'lattice strain' model equation are given in Table 4. For each perovskite, E_α still increases with defect charge, and interestingly, now r_0 follows the experimental trend observed in the partition coefficients (D), i.e., it decreases with increasing defect charge (Fig. 5). Although the order $r_0(MgSiO_3) < r_0(CaSiO_3)$ expected from crystal chemistry is observed and the experimental trend in the D values now followed, simulated r_0 values are somewhat smaller than the ones derived from experiment (Fig. 5). The experimental work was carried out on (Mg, Fe)SiO_3 perovskite rather than pure $MgSiO_3$ perovskite and this could have contributed to this discrepancy, Fe^{2+} being slightly larger than Mg. It is clear that more similarities are found between simulation and experimental approaches when considering solution than relaxation energies. This observation, seen previously for other silicates (e.g., Van Westrenen et al., 2000), suggests a non-negligible contribution made by melt in the partitioning of trace elements. Experimental results for $CaSiO_3$ perovskite suggest that E_α remains constant with increasing cation charge (Fig. 5). This observation contrasts with the results of our simulations and the experimental trend reported for $MgSiO_3$ perovskite (this study), garnet (Van Westrenen et al., 1999) and wollastonite (Law et al., 2000). Confirmation or rejection of this discrepancy will be possible as more experimental partitioning data become available.

5.3. Effect of trace element environments in melt

To estimate solution energies above, we made the particularly simple assumption that the local environment of the trace and host cations in the melt is equivalent to their environment in the corresponding simple oxides. As previously done by Van Westrenen et al. (2000), we decided to study the effect a different melt environment could have on U_{sol}^{3+} by assuming a YAG-type (yttrium-aluminium-garnet: $Y_3Al_5O_{12}$) environment for trivalent trace elements in the melt.

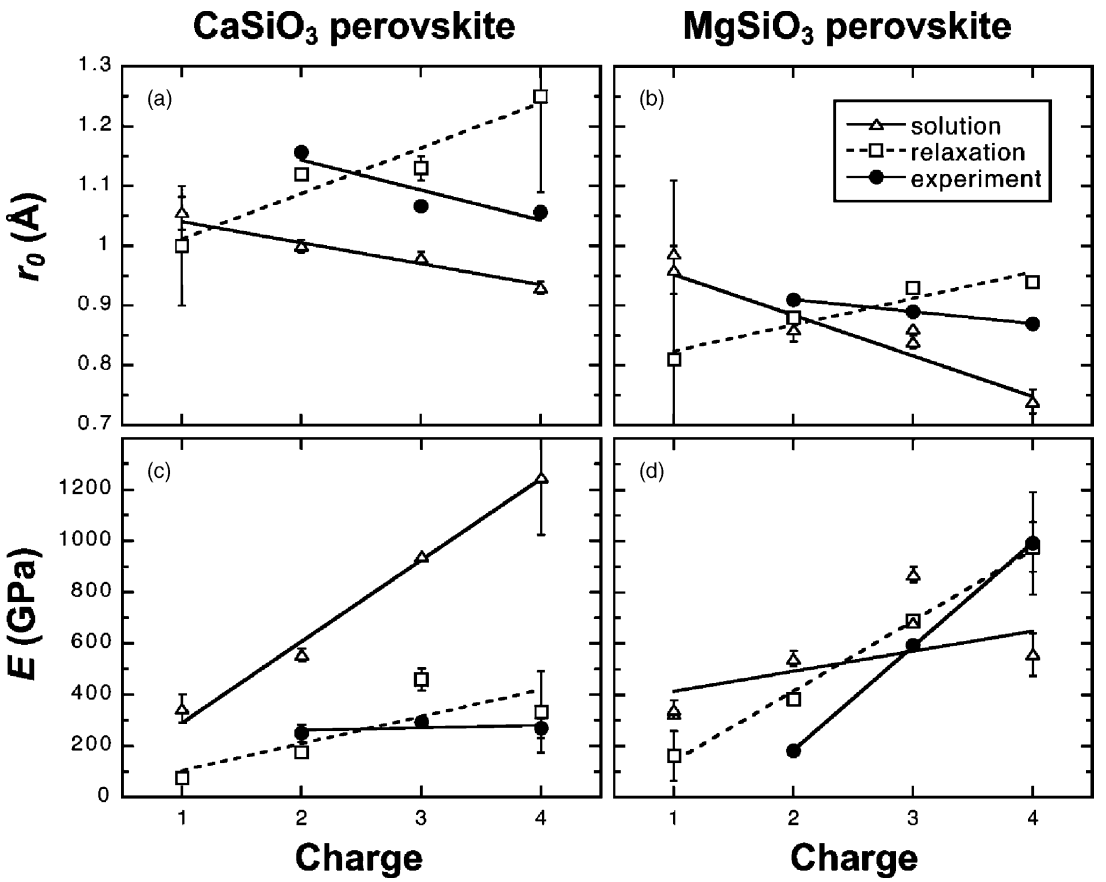

Fig. 5. Fitted values of (a–b) r_0 and (c–d) E_α as a function of defect charge for relaxation and solution energies in $CaSiO_3$ and $MgSiO_3$ perovskite. Data are taken from Table 4. Fits to experimental data are also shown for comparison.

We considered the following exchange reactions:

$$\tfrac{1}{3}M_3Al_5O_{12} + \tfrac{1}{2}Li_2O + 2Mg_{Mg} \Leftrightarrow Li'_{Mg} + M^{\bullet}_{Mg} + 2MgO + \tfrac{5}{6}Al_2O_3 \quad (12a)$$

$$U_{sol} = U_{def,f}(M'_{Mg} + Li^{\bullet}_{Mg}) + 2U_{lat}(MgO) + \tfrac{5}{6}U_{lat}(Al_2O_3) - \tfrac{1}{2}U_{lat}(Li_2O) - \tfrac{1}{3}U_{lat}(M_3Al_5O_{12}) \quad (12b)$$

$$\tfrac{1}{3}M_3Al_5O_{12} + Ca_{Ca} + Si_{Si} \Leftrightarrow M^{\bullet}_{Ca} + Al'_{Si} + CaO + SiO_2 + \tfrac{1}{3}Al_2O_3 \quad (13a)$$

$$U_{sol} = U_{def,f}(M^{\bullet}_{A} + Al'_{Si}) + U_{lat}(CaO) + U_{lat}(SiO_2) + \tfrac{1}{3}U_{lat}(Al_2O_3) - \tfrac{1}{2}U_{lat}(M_3Al_5O_{12}) \quad (13b)$$

The coordination number of M^{3+} in the melt component is now 8, as compared with 6 in the case of the simple oxide environment. This is obviously an extreme case, and we do not propose that trivalent cations normally have this environment in silicate melt. Lattice energies for YAG-type components, corresponding solution energies and regression parameters E_α and r_0 of the 'lattice strain' model fits are given in Table 5. As shown in Fig. 6, the near-parabolic dependence of U_{sol} on ionic radius is preserved. However, E_α^{3+} values are lower by a factor of two. In addition, ${r_0}^{3+}$ for $MgSiO_3$ perovskite is significantly lower when assuming a YAG-type melt environment rather than a simple oxide environment. It is clear that, although trends of apparent E_α and r_0 are directly related to the crystal chemistry, their absolute values do depend on the nature and coordination

Table 5
Solution energies assuming a YAG-type environment in melt[a]

Defect	$U_{lat}(M_3Al_5O_{12})$	Solution energy, U_{sol}	
		$MgSiO_3$	$CaSiO_3$
Al_A^{3+}	−61781	75	113
Fe_A^{3+}	−60534	95	45
Sc_A^{3+}	−59855	115	−19
Lu_A^{3+}	−58859	177	−54
Yb_A^{3+}	−58731	188	−52
Ho_A^{3+}	−58432	215	−54
Gd_A^{3+}	−58001	261	−46
Eu_A^{3+}	−57904	272	−44
Nd_A^{3+}	−57511	321	−29
Pr_A^{3+}	−57278	354	−20
La_A^{3+}	−56975	400	1
r_0 (Å)		0.69 (1)	1.00 (1)
E_α (GPa)		389 (20)	489 (27)

[a] Energies in kJ/mol.

of the phase with which the trace element is being exchanged, as Van Westrenen et al. (2000) suggested for end-member garnets. Considering the E_α^{3+} and r_0^{3+} values, it appears that, of the two assumptions of melt environment, here the binary oxide assumption shows the best agreement with the experimental observations.

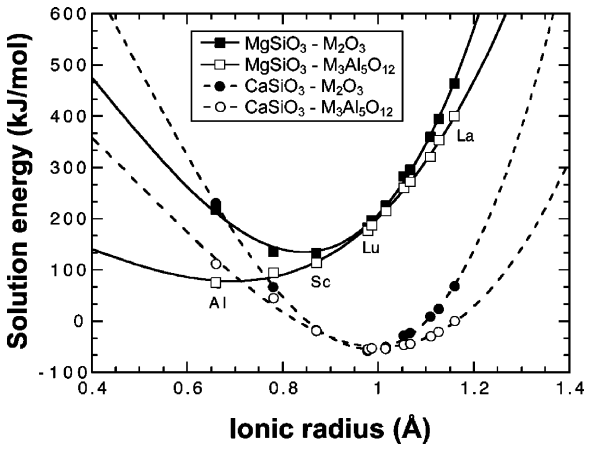

Fig. 6. Calculated solution energies for trivalent cation incorporation in $MgSiO_3$ and $CaSiO_3$ perovskite assuming two types of local melt environment (M_2O_3 and $M_3Al_5O_{12}$). Data for YAG-type melt environment are given in Table 5.

5.4. Relationship between solution energies and partition coefficients

An important issue is the relationship between partition coefficients and solution energies. Equations of the form of Eq. (1) can be applied with success to the variation of both partition coefficients and solution energies with ion size for a given charge. Furthermore, D and U_{sol} values are consistent when comparing the incorporation of a given element in the two perovskites. As an illustration, we find, whatever the substitution mechanisms envisaged, the order $U_{sol}(MgSiO_3) > U_{sol}(CaSiO_3)$ for U^{4+}, Th^{4+}, REE^{3+}, Sr^{2+} and Ca^{2+} which agrees with $D(MgSiO_3) < D(CaSiO_3)$ for all these elements. This relationship is true for all elements for which D and U_{sol} are available. Thus, since $U_{sol}(MgSiO_3) > U_{sol}(CaSiO_3)$ for Li^+, Na^+, K^+ and Rb^+, we would expect to have $D(MgSiO_3) < D(CaSiO_3)$ for these elements also.

Comparing D values in a given perovskite for ions of different charge is more problematic. Calculated solution energies reflect small differences between a number of large quantities. Many of these quantities (e.g., binary lattice energies) do not differ with trace element size for a given charge but do vary with trace element charge since the solution mechanism changes. Calculated variations in solubility with size for a given charge are therefore expected to be more reliable than those with charge for a given size. For example, in $MgSiO_3$ perovskite, $U_{sol}(Mg^{2+}) < U_{sol}(Sc^{3+})$, leading to anticipated $D_{Mg} > D_{Sc}$, whereas experimentally $D_{Mg} < D_{Sc}$.

6. Conclusions

The successful application of the ‘lattice strain’ model to our simulated relaxation and solution energies underlines the important contribution made by the crystal chemistry to the partitioning of trace elements between both perovskites and melt. This is in good agreement with the experimental perovskite–melt partitioning observations. As noted by Van Westrenen et al. (2000) in simulations of trace element incorporation in garnet, solution energies are more consistent with the experimental observations than relaxation energies. For example, r_0 values derived from the fitting of solution energies in perovskite decrease

with increasing defect charge. This trend, contrary to the one observed from consideration of relaxation energies, is consistent with experiment, and so far appears to be a general feature of element partitioning into minerals. Considering solution energies, our conclusions are:

(1) For a given trace element charge $r_0(MgSiO_3) < r_0(CaSiO_3)$, as observed experimentally.
(2) E_α values increase with increasing trace element charge, as observed experimentally for $MgSiO_3$ perovskite–melt partitioning.
(3) Solution energies and thus r_0 and E_α values derived from the fitting of solution energies are sensitive to the local environment of trace elements in the melt.
(4) For trivalent and tetravalent cation incorporation in the large site of both perovskites, solution energies for envisaged substitution mechanisms are close to one other, and it is therefore difficult to conclude in favour of only one mechanism.
(5) Whatever the mechanism of charge compensation considered, solution energies for REE^{3+}, and tetravalent cations (including U^{4+} and Th^{4+}) are much lower in $CaSiO_3$ perovskite than in $MgSiO_3$ perovskite. This feature alone could explain the large difference in optimum partition coefficients D_0^{3+} and D_0^{4+} for the large site between the two perovskites. Different substitution mechanisms for the two perovskites are not required.
(6) D and U_{sol} values are consistent when comparing the incorporation of a given element in the two perovskites. For example, $D_i(CaSiO_3) > D_i(MgSiO_3) \Leftrightarrow U_{sol,i}(CaSiO_3) < U_{sol,i}(MgSiO_3)$. However, further refinement of the theoretical model is required to investigate accurately differences in solution energies in a given mineral for ions of the same size but different charge.

Further work should be directed towards: (1) improving the partitioning data set for both $MgSiO_3$ and $CaSiO_3$ perovskite–melt which would enable us to constrain E_α and r_0 values better over a range of melt compositions; this will also allow us to resolve the apparent discrepancy for $CaSiO_3$ in the variation of E_α with charge between theory and experiment; (2) explicit calculation of defect and solution energies via supercell technique rather than the Mott–Littleton approach in order to assess the effects of high pressure on these quantities; (3) performing direct simulation at high temperatures of trace element partitioning using Monte Carlo calculations (Purton et al., 2000; Allan et al., 2001, 2003).

Acknowledgements

AC acknowledges the support of a postgraduate scholarship from the University of Bristol. The original manuscript benefited from reviews by R. Trønnes, K. Hirose and W. Van Westrenen.

References

Allan, N.L., Blundy, J.D., Purton, J.A., Lavrentiev, M.Y., Wood, B.J., 2001. Trace element incorporation in minerals and melts. In: Geiger, C.A. (Ed.), Solid Solutions in Silicate and Oxide Systems of Geological Importance. EMU Notes in Mineralogy, vol. 3, No. 11, pp. 251–302.

Allan, N.L., Du, Z., Lavrentiev, M.Yu., Blundy, J.D., Purton, J.A., Van Westrenen, W., 2003. Atomistic stimulation of mineral-melt trace-element partitioning. Phys. Earth Planet. Int. This issue.

Aylward, G., Findlay, T., 1994. SI Chemical Data, 3rd ed. Wiley, New York.

Blundy, J.D., Wood, B.J., 1994. Prediction of crystal–melt partition coefficients from elastic moduli. Nature 372, 452–454.

Brice, J.C., 1975. Some thermodynamic aspects of the growth of strained crystals. J. Crystal Growth 28, 249–253.

Buscaglia, M.T., Buscaglia, V., Viviani, M., 2001. Atomistic simulation of dopant incorporation in barium titanate. J. Am. Ceram. Soc. 84, 376–384.

Catlow, C.R.A., Mackrodt, W.C., 1982. Theory of simulation methods for lattice and defect energy calculations in crystals. In: Catlow, C.R.A., Mackrodt, W.C. (Eds.), Computer Simulation of Solids. Springer, Berlin, pp. 3–20.

Corgne, A., Wood, B.J., 2002. $CaSiO_3$ and $CaTiO_3$ perovskite–melt partitioning of trace elements: implications for gross mantle differentiation. Geophys. Res. Lett. 29, 1903. doi: 10.1029/2001GL014398.

Dick, B.G., Overhauser, A.W., 1958. Theory of the dielectric constants of alkali halide crystals. Phys. Rev. 112, 90–103.

Gale, J.D., 1997. GULP: a computer program for the symmetry adapted simulation of solids. Faraday Trans. 93, 629–637.

Hartmann, W.K., Davis, D.R., 1975. Satellite-sized planetesimals and lunar origin. Icarus 24, 504–515.

Herzberg, C.T., O'Hara, M.J., 1985. Origin of mantle peridotite and komatiite by partial melting. Geophys. Res. Lett. 12, 541–544.

Hill, E., Wood, B.J., Blundy, J.D., 2000. The effect of Ca–Tschermaks component on trace element partitioning between clinopyroxene and silicate melt. Lithos 53, 203–215.

Hirose, K., Shimizu, N., Van Westrenen, W., Fei, Y., in press. Trace element partitioning in Earth's lower mantle and implications for geochemical consequences of partial melting at the core–mantle boundary. Phys. Earth Planet. Int.

Horiuchi, H., Ito, E., Weidner, D., 1987. Perovskite type $MgSiO_3$: single crystal X-ray diffraction study. Am. Mineral. 72, 357–360.

Knittle, E., Jeanloz, R., 1987. Synthesis and equation of state of (Mg, Fe)SiO_3 perovskite to over 100 gigapascals. Science 235, 668–670.

Kröger, F.A., Vink, H.J., 1956. Relations between the concentrations of imperfections in crystalline solids. Solid State Phys. 3, 307–435.

Law, K.M., Blundy, J.D., Wood, B.J., Ragnarsdottir, K.V., 2000. Trace element partitioning between wollastonite and silicate–carbonate melt. Mineral. Mag. 64, 155–165.

Lewis, G., Catlow, C.R.A., 1985. Potential models for ionic oxides. J. Phys. C 18, 1149–1161.

Mott, N.F., Littleton, M.T., 1938. Conduction in polar crystals. I. Electrolytic conduction in solid salts. Trans. Faraday Soc. 34, 485–499.

Ohtani, E., 1985. The primordial terrestrial magma ocean and its implications for stratification of the mantle. Earth Planet. Sci. Lett. 78, 70–80.

Purton, J.A., Allan, N.L., Blundy, J.D., Wasserman, E.A., 1996. Isovalent trace element partitioning between minerals and melts—a computer simulation model. Geochim. Cosmochim. Acta 60, 4977–4987.

Purton, J.A., Allan, N.L., Blundy, J.D., 1997. Calculated solution energies of heterovalent cations in forsterite and diopside: implications for trace element partitioning. Geochim. Cosmochim. Acta 61, 3927–3936.

Purton, J.A., Blundy, J.D., Allan, N.L., 2000. Computer simulation of high temperature forsterite–melt partitioning. Am. Mineral. 87, 1087–1091.

Ringwood, A.E., 1979. Origin of the Earth and Moon. Springer, New York.

Sanders, M.J., Leslie, M., Catlow, C.R.A., 1984. Interatomic potentials for SiO_2. J. Chem. Soc. Commun., 1271–1274.

Shannon, R.D., 1976. Revised effective ionic radii and systematic studies of interatomic distances in halides and chalcogenides. Acta Cryst. A 32, 751–767.

Shim, S.-H., Duffy, T.S., Shen, G., 2000. The stability and P–V–T equation of state of $CaSiO_3$ perovskite in the earth's lower mantle. J. Geophys. Res. 105, 25955–25968.

Taylor, M.B., Barrera, G.D., Allan, N.L., Barron, T.H.K., Mackrodt, W.C., 1997. Free energy of formation of defects in polar solids. Faraday Discuss. 106, 377–387.

Van Westrenen, W., Blundy, J.D., Wood, B.J., 1999. Crystal-chemical controls on trace element partitioning between garnet and anhydrous silicate melt. Am. Mineral. 84, 838–847.

Van Westrenen, W., Allan, N.L., Blundy, J.D., Purton, J.A., Wood, B.J., 2000. Atomistic simulation of trace element incorporation into garnets—comparison with experimental garnet–melt partitioning data. Geochim. Cosmochim. Acta 64, 1629–1639.

Wang, Y., Weidner, D.J., Guyot, F., 1996. Thermal equation of state of $CaSiO_3$ perovskite. J. Geophys. Res. 101, 661–672.

Watson, G.W., Wall, A., Parker, S.C., 2000. Atomistic simulation of the effect of temperature and pressure on point defect formation in $MgSiO_3$ perovskite and the stability of $CaSiO_3$ perovskite. J. Phys. Condens. Matter 12, 8427–8438.

Wright, K., Price, D.P., 1993. Computer simulation of defects and diffusion in perovskites. J. Geophys. Res. 98, 22245–22253.